Author Manuscript

Author Manuscript

Author Manuscript

Author Manuscript

HHS Public Access

Author manuscript

Nat Methods. Author manuscript; available in PMC 2021 October 05.

Published in final edited form as:

Nat Methods. 2021 April ; 18(4): 417–425. doi:10.1038/s41592-021-01104-8.

Miniaturized head-mounted microscope for whole cortex mesoscale imaging in freely behaving mice

Mathew L Rynes[1,*], **Daniel Surinach**[2,*], **Samantha Linn**[2], **Michael Laroque**[3], **Vijay Rajendran**[2], **Judith Dominguez**[2], **Orestes Hadjistamolou**[2], **Zahra S Navabi**[2], **Leila Ghanbari**[2], **Gregory W Johnson**[2], **Mojtaba Nazari**[4], **Majid Mohajerani**[4], **Suhasa B Kodandaramaiah**[1,2,5,^]

[1]Department of Biomedical Engineering, University of Minnesota Twin Cities

[2]Department of Mechanical Engineering, University of Minnesota Twin Cities

[3]Schools of Medicine, University of Minnesota Medical School

[4]Department of Neuroscience, Canadian Centre for Behavioural Neuroscience, University of Lethbridge, Lethbridge, AB, Canada

[5]Department of Neuroscience, University of Minnesota, Twin Cities

Abstract

The advent of genetically encoded calcium indicators, along with surgical preparations such as thinned skulls or refractive index matched skulls, have enabled mesoscale cortical activity imaging in head-fixed mice. However, neural activity during unrestrained behavior substantially differs from neural activity in head-fixed animals. For whole-cortex imaging in freely behaving mice, we

Users may view, print, copy, and download text and data-mine the content in such documents, for the purposes of academic research, subject always to the full Conditions of use: http://www.nature.com/authors/editorial_policies/license.html#terms

[^]**Send manuscript correspondence to:** Suhasa B Kodandaramaiah, Department of Mechanical Engineering, University of Minnesota, Twin Cities, **Address:** 111 Church St SE, Room 303, Minneapolis, MN 55455, suhasabk@umn.edu.

[*]Equal Contribution

AUTHOR CONTRIBUTIONS

MLR, LG, ML, DS, LG, GJ, SBK designed and engineered the mini-mScope. MLR, DS, JD, ZSN, OH, LG, SBK designed and executed the experiments. MLR, DS, SL, OH, VR and SBK analyzed the data. MLR, DS, SL, VR, JD, ML, SBK wrote the manuscript. MN and MM designed, executed glutamate imaging experiments and analyzed the data and assisted with manuscript writing.

Editor summary: The mini-mScope is a miniature microscope that can image neural activity at the mesoscale in most of the dorsal cortex of freely behaving mice.

Editor recognition statement: Peer review information: Nina Vogt was the primary editor on this article and managed its editorial process and peer review in collaboration with the rest of the editorial team.

Reviewer recognition statement: Nature Methods thanks Ariel Gilad, Ashok Veeraraghavan, and Denise Cai, for their contribution for the peer review of this work.

COMPETING INTERESTS

The authors declare no competing interests.

Data Availability

Source data for plots in figures (except for videos, pseudocolor maps, and images) are provided with this paper. Data containing videos, pseudocolor maps, and images are available upon request from the authors due to large file sizes. The Allen Brain Atlas was used as an anatomical reference for data analysis in this study (http://www.brain-map.org). All CAD files for fabricating the mini-mScope are available with this article as Supplementary Data 2.

Code Availability

All custom codes are available on Github at https://github.com/bsbrl/mini-mScope.

Author Manuscript Author Manuscript Author Manuscript Author Manuscript

here present the “mini-mScope,” a wide-field, miniaturized, and head-mounted fluorescence microscope compatible with transparent polymer skull preparations. With a field of view of 8 mm x 10 mm and weighing less than 4 g, the mini-mScope can image most of the mouse dorsal cortex with resolution ranging from 39 to 56 μm. We have used the mini-mScope to record mesoscale calcium activity across the dorsal cortex during sensory-evoked stimuli, open field behaviors, social interactions, and transitions from wakefulness to sleep.

INTRODUCTION

Genetically encoded calcium indicators[1], along with transgenic approaches for broadly expressing these indicators in the brain in a cell-type specific fashion[2] has enabled mesoscale imaging of multiple cortical regions simultaneously[3]. These studies have revealed how neural activity across several regions of the cortex are coordinated in a variety of brain states and behaviors[4–8]. These studies have thus far been mostly done in head-fixed mice[9,10]. Even relatively simple behaviors in head-fixed animals require substantial time for acclimatization and training[11]. To overcome some limitations of head-fixation, immersive virtual reality environments[12] or voluntary head-fixation of mice in their home cages[13] have been used in mesoscale imaging studies. However, the lack of vestibular inputs and disruptions in eye-head movement coupling[14], and behavioral effects from increased stress[15] can alter neural activity during head-fixation[16].

Several head-mounted, miniaturized imaging devices have been developed for cellular-resolution imaging of neural activity from small fields of view (FOV, < 1 mm^2) in freely moving animals[17–19]. A head-mounted imaging device with a relatively large FOV has recently been engineered for mesoscale imaging in rats[20]. In comparison to rats, mice have a much larger slate of genetic tools[21–23]. A miniaturized, head-mounted device with a large FOV for imaging the whole cortex in mice has the potential to expand investigations of mesoscale cortical dynamics during free behavior.

Here, we introduce the “mini-mScope,” a miniature imaging device capable of simultaneously imaging an 8 x 10 mm FOV with resolution ranging from 39.37 to 55.68 μm. The mini-mScope weighs 3.8 g and can be head-borne by a freely moving mouse. We have used the mini-mScope to record mesoscale cortical activity in freely behaving solitary mice and during social interactions with a companion mouse.

RESULTS

Mini-mScope Design

The mini-mScope design was constrained by three criteria. First, the overall weight of the device needed to be less than ~15% of the mouse bodyweight (<4.0 g) to permit free behavior and mobility. Second, the device required the capability to image most of the dorsal cortex of the mouse. Third, the imaging resolution needed to be sufficient to image mesoscale activity dynamics across the whole FOV. We recently developed See-Shells–transparent polymer skulls that can be chronically implanted on mice and provide access to 45 mm^2 of the dorsal cortex[24] in head-fixed animals. In this study, we adapted the See-Shell

Author Manuscript Author Manuscript Author Manuscript Author Manuscript

to fit the mini-mScope by incorporating a planar top surface in the 3D printed frame, eliminating the headpost, and incorporating three tabs. Disk magnets were embedded in the two lateral tabs to align with disk magnets on the bottom of the mini-mScope or a protective cap (Fig. 1a). A short sleeve surrounding the mini-mScope base and the posterior tab in the bottom housing constrains the mini-mScope laterally once mounted on the See-Shell. The tab at the back of the See-Shell frame was used to gently restrain the mouse during removal of the protective cap and attachment of the mini-mScope. Attaching the mini-mScope typically takes less than 5 seconds and can be done without anesthetizing the mouse.

The mini-mScope consists of two interlocking computer numerical control (CNC) machined Delrin housings (Fig. 1a). Three blue LEDs paired with an excitation filter are installed into three illumination arms in the bottom housing (Fig. 1b). A green LED provides illumination for reflectance measurements. A biconvex lens and emission filter are embedded in a central shaft of the bottom housing. A complementary metal oxide semiconductor (CMOS) sensor is mounted on the top housing, which is designed to slide along the central square shaft of the bottom housing for focus adjustments. The three blue LEDs are wired in series, and wires to power the green and blue LEDs are routed through a commutator to alleviate torsional strain on the device. Mice exhibited a repertoire of behaviors, including grooming and rearing, indicating their comfort with the mini-mScope (Fig. 1b, Supplementary Video 1).

The weight of the device is 3.8 g, which is heavier than some miniaturized microscopes[17], but comparable to devices developed for volumetric imaging[19]. Based on computer-aided design (CAD) simulations, we estimate that the center of gravity is ~24.7 mm above the mouse head. Detailed instructions for assembling the mini-mScope are provided in Supplementary Figure 1 and Supplementary Note 1.

Mini-mScope Optical Performance

In contrast to typical imaging through a reinforced intact skull, the mini-mScope images the cortex through a transparent polymer skull. Qualitatively, imaging the cortex of a Thy1-GCaMP6f mouse[23], which expresses fluorescent reporters of calcium activity in excitatory neurons, with the mini-mScope allowed us to achieve a high optical resolution across the FOV (Fig. 1c) compared to imaging the cortex through the intact skull using an epifluorescence macroscope (Fig. 1d). To measure the mini-mScope's resolution, we imaged a 1951 USAF resolution test target positioned at 8 different locations across the FOV (Fig. 1e). At a location corresponding to ~ −5.5 mm anteroposterior (AP), ~0 mm mediolateral (ML) with respect to Bregma, lines in group 3, element 6 are clearly visible, indicating a resolution of 39.36 μm at this location. Since a single biconvex lens was used to image a convex surface, not all areas of the cortex are in focus and the optical resolution varied. The top housing was adjusted to obtain the best focus at ~1 mm lateral to the midline, resulting in resolution ranging from 39 μm along the midline to 55.6 μm more laterally, sufficient for observing mesoscale calcium activity.

The mini-mScope's array of three blue LEDs paired with excitation filters delivered a cumulative ~31 mW of power to the brain (Supplementary Fig. 2). Two of the blue LEDs are oriented at 30 degrees with respect to the optical axis. The third, located at the anterior of the

Author Manuscript Author Manuscript Author Manuscript Author Manuscript

bottom housing, is oriented at 25 degrees with respect to the optical axis. The LEDs are revolved around the optical axis at angles of 90, 225, and 315 degrees (Supplementary Fig. 2b). A green LED located at the posterior of the bottom housing at an orientation of 55 degrees with respect to the optical axis delivered ~0.22 mW of power and was used for reflectance measurements[25]. We imaged fluorescein dye-infused agar gel using the mini-mScope to investigate illumination uniformity (Fig. 1f). The normalized light intensity decreased by 56.1%, 53.3%, and 46.2%, compared to the maximum intensity, at the ML lines at 1.4 mm AP, −2.8 mm AP, and −4.2 mm AP, respectively (Fig. 1g). The greatest reduction of illumination from the maximum did not exceed 60%. These metrics are comparable to the performance of previously developed large FOV scopes[20], and allowed signals obtained from all pixels to be well within the dynamic range of the CMOS sensor.

The CMOS sensor captures images of the cortex alternatively illuminated by the green LED for reflectance imaging and the blue LEDs for epifluorescence imaging. A trigger circuit uses time stamps of CMOS frame acquisitions to precisely switch between the blue LEDs and green LED (Supplementary Fig. 2c–e). The circuit and LEDs have first-order dynamics with the blue LEDs and green LED having time constants (to reach 66.66% peak power) of 1.79 ± 0.31 ms and 1.97 ± 0.10 ms, respectively. The Blue LEDs and green LED were switched on for 20 ms and 4 ms, respectively, starting after the CMOS sensor initiated each frame capture. The LEDs' power intensity had a slow drift in average intensity value lasting ~2 minutes after which they equilibrated (Supplementary Fig. 2f, Supplementary Note 2). Therefore, we allocated a two-minute warmup period for the blue LEDs during each experiment for the power intensity to stabilize before data collection.

Comparison with conventional epi-fluorescence macroscope

We next compared the mini-mScope's imaging capabilities to a standard epifluorescence macroscope by imaging spontaneous cortical activity under anesthesia. Despite substantial differences in the capability of the optics and the image sensors, we captured qualitatively comparable widefield images and calcium activity with both instruments (Fig. 2 a–b). We observed heart beat-related oscillations in the calcium signals at 6-7 Hz in the imaging performed with both instruments (Fig 2c). The histograms of ΔF/Fs and z-score of intensity values acquired from three regions of interest (ROIs) show minimal differences between the data captured from the two instruments (Fig. 2 d–e). The probability of ΔF/F values being over 1 standard deviation from the mean was 31.7% for the mini-mScope and 30.2% for the conventional macroscope. Green reflectance channel imaging allowed correction of the calcium fluorescent signals for hemodynamic effects (Fig. 2 f–g). We also benchmarked the signal-to-noise ratio (SNR) of the two instruments by imaging stimulus evoked activity. The mini-mScope does have a reduced SNR, owing to the lower quantum efficiency of the mini-mScope's CMOS sensor (Supplementary Fig. 3, Supplementary Note 3). Further, the mini-mScope was also able to perform imaging through a modified intact skull (Supplementary Fig. 4, Supplementary Note 4). These results demonstrate that the mini-mScope can acquire calcium signals that are comparable to a conventional epifluorescence macroscope.

Author Manuscript Author Manuscript Author Manuscript Author Manuscript

Imaging sensory stimulus evoked responses across the cortex

Stimulating distinct sensory pathways evokes neural activity in specific primary sensory areas located within the dorsal cortex. Providing a mouse under light (<1%) isoflurane anesthesia with a series of brief vibrational stimuli (1s long, 100 Hz) to the right hind limb (Fig. 3a), evoked robust calcium activity in the contralateral hind limb (HL) region of the somatosensory cortex within 500 ms of the onset of stimulus (Fig. 3b–c). The peak post stimulus response was 1.68% ± 0.49% ΔF/F (Fig. 3d, n = 17 trials in 1 mouse). In comparison, the peak post-stimulus response on the ipsilateral side was significantly lower (0.70% ± 0.34% ΔF/F, Fig. 3e–f, $\alpha = 0.05$ for significance, $p = 9.1x10^{-3}$, paired t-test). We presented the same mouse with 100 ms long flashes of white light to the left eye (Fig. 3g), evoking a robust increase in calcium activity in the contralateral visual cortex (Fig. 3h–i). The peak post stimulus response was 1.7% ± 0.32% ΔF/F (Fig. 3j, n = 18 trials). In comparison, the peak post-stimulus response on the ipsilateral visual cortex was significantly lower (0.38% ± 0.057% ΔF/F, Fig. 3k–l, $\alpha = 0.05$ for significance, $p = 1.31x10^{-5}$, paired t-test). Thus, the mini-mScope can reliably measure evoked responses to varied sensory stimuli in both hemispheres of the dorsal cortex. We performed experiments to test whether visual and auditory stimulus evoked activity could be measured in mice freely locomoting in an open field. The responses were more variable owing to the awake state, but we nevertheless obtained distinct responses (Supplementary Fig. 5, Supplementary Note 5).

Effect of mounting a mini-mScope on behavior and imaging stability

We next assessed if either implanting the see-shell or mounting the mini-mScope affected behavior in both long-term and short-term experiments. We found that mice implanted with the see-shell and mice implanted with the see-shell and fitted with the mini-mScope exhibited similar measures of agility and locomotion when compared to control mice (Supplementary Fig. 6, Supplementary Note 6). We also assessed the stability of the images captured using the mini-mScope during free behavior (Supplementary Video 2). The absolute maximum x and y displacements of the FOV were 21.0 ± 21.8 μm and 14.4 ± 17.1 μm (Supplementary Fig. 7, Supplementary Note 7). These displacements could be corrected for digitally using the MoCo correction algorithm[26]. We also observed large changes (up to 25%) in diameter of the superior sagittal sinus (SSS, Supplementary Fig. 8, Supplementary Note 7). These variations could introduce artifacts in the analysis of the calcium signals. Thus, we removed areas close to the SSS from the FOV prior to analyses.

Mapping cortical functional connectivity during open field exploration and social interactions

We used the mini-mScope to examine functional connectivity between cortical areas during open field behavior of solitary mice and during social interactions with a companion mouse (Fig. 4a–b). We segregated solitary open field trials into four types of behaviors – periods when mice were still, moving, grooming, or rearing. On average, mice spent 70.6% ± 9.0% of the time remaining still (n = 11 trials, 3 mice), while spending 20.7% ± 7.51% of the time moving within the arena. Grooming and rearing were less frequent and shorter in durations, accounting for 7.7% ± 6.02% and 1.04% ± 1.17% of the time respectively (Fig. 4c). To

Author Manuscript Author Manuscript Author Manuscript Author Manuscript

study social behavior, we allowed mice bearing the mini-mScope to first explore the arena before we introduced a companion mouse of the same sex (n = 8 trials, 8 mice, Supplementary Video 3). Mice spent 41.3% ± 19.5% of time socially interacting with each other, including touching whiskers or the body (Fig. 4d).

We constructed hemodynamics-corrected seed-pixel correlation maps of the cortex from the calcium activity videos during open field behavior. We analyzed maps with respect to six seeds within the motor cortex (M1), the forelimb (FL), the hind limb (HL), and the barrel cortex (BC) areas in the somatosensory cortex, the retrosplenial cortex (RSC), and the visual cortex (VC) (Fig. 4e, f). Correlations between the seed locations changed when the animal was moving versus still. Between the seeds, correlations increased, particularly between those located within the somatosensory cortex. The area of the left hemisphere of the cortex that is highly correlated with respect to a given seed location, increased for all seeds analyzed when the animal was moving (Fig. 4g) and these increases were found to be significantly higher for seeds located at M1, HL, FL, VC and RSC (n = 11 trials, 3 mice, α = 0.05 for significance, p = $4.6x^{-3}$ M1, p = $6.3x10^{-4}$ FL, p = $3.8x10^{-3}$ HL, p = $4.6x10^{-3}$ RSC, p = 0.10 BC, p = $1.1x10^{-3}$ VC, Mann-Whitney U-test). Overall, movement induced increased variance in the inter-seed correlations (Fig. 4h). Similarly, we constructed seed-pixel correlation maps for mice engaging in social behaviors (Fig. 4i). Intra-cortical connectivity was increased during times where the mice were engaged in social behaviors (Fig. 4i–k, n=8 mice, α = 0.05 for significance, p = 0.048 M1, p = 0.17 FL, p = 0.058 HL, p = 0.091 RSC, p = 0.082 BC, p = 0.37 VC, Mann-Whitney U-test). These results demonstrate the utility of the mini-mScope to study functional connectivity during behaviors that are unique to freely behaving mice.

Imaging glutamate release dynamics during wakefulness and natural sleep

As a final demonstration, we used the mini-mScope to measure dynamic changes in extracellular glutamate release in the cortex during transition from wakefulness to natural sleep. Much of the previous work studying extracellular glutamate release has been done using fixed-potential amperometry[27], or optical imaging in head-fixed mice[28]. Inducing sleep in head-fixed mice is challenging and typically requires sleep deprivation which can alter the overall sleep structure and patterns of rapid eye-movement (REM) and non-REM (NREM) sleep[29,30]. The flexibility of the See-Shells allowed us to incorporate local field potential (LFP) recording electrodes in the dorsal hippocampus in Emx-CaMKII-Ai85 mice, expressing iGluSnFR in glutamatergic neocortical neurons[22]. We allowed mice to naturally transition to sleep in their home cage and recorded glutamate activity across the whole dorsal cortex during wakefulness, REM sleep, and NREM sleep (Fig. 5). Hippocampal LFP indicated transition to NREM sleep characterized by high amplitude slow waves (0.5-4 Hz) and subsequently REM sleep characterized by theta band activity (7 – 9 Hz, Fig. 5b–c,h). Consistent with previous studies, spontaneous cortical activity patterns during quiet wakefulness and NREM were highly synchronized across hemispheres[31]. In addition, cortical activity changes were not necessarily due to global changes in state, and were instead composed of complex local activity patterns (Fig. 5a). The transition from wakefulness to NREM sleep and REM sleep resulted in decreased fluorescence, indicating reduced cortical glutamate activity (Fig. 5a–d). We also observed a reduction of slow

Author Manuscript Author Manuscript Author Manuscript Author Manuscript

cortical glutamate fluctuations during REM sleep (Fig. 5e). Correlation analysis of cortical activity revealed that connectivity decreases in REM sleep compared to quiet wakefulness and NREM sleep (Fig. 5f–g). Moreover, consistent with previous studies, the strength of functional connectivity was less in NREM sleep compared to quiet wakefulness[31]. The mini-mScope attachment also allowed us to study the transition from REM sleep to wakefulness, wherein we observed increased glutamate activity across the cortex (Fig. 5h–i).

DISCUSSION

We have introduced a neurotechnology for mesoscale activity mapping of the dorsal cortex in freely behaving mice.

Among mammalian models used in neuroscience, mice have the widest range of transgenic animals for broad expression of genetically encoded calcium indicators[23,32,33], voltage indicators[2] as well as reporters of neurotransmitters[34]. Combined with mouse models of neurodegenerative and neuropsychiatric disorders[35], the mini-mScope should enable studies of mesoscale cortical activity mediating a range of complex behaviors in healthy mice and how these activities may be disrupted in diseased states.

The mini-mScope utilizes the CMOS sensor used in the open source “miniscope”[36]. The miniscope platform is rapidly evolving, and sensors with increased sensitivity and imaging speed[37], miniaturization, and wireless imaging capabilities[38] are being developed. While the current mini-mScope’s SNR is reduced when compared to the conventional epifluorescence macroscope, future versions could incorporate these improved sensors which are optimized for imaging dim voltage indicators[37].

The mini-mScope performs reflectance measurements at green wavelengths to correct for hemodynamic effects. Multiple wavelength reflectance measurements allow more accurate correction of hemodynamic effects[25,39]. In future versions, an additional red LED could be incorporated to obtain reflectance measurements at two wavelengths. Alternatively, issues with hemodynamic corrections could be addressed by illuminating GCaMP6f at its isosbestic point[40]. The mini-mScope architecture can also be adapted to image red-shifted fluorescent reporters where hemodynamic effects are not prevalent[41].

The mini-mScope’s FOV is currently limited to the dorsal cortex. Future mini-mScopes could be designed with an expanded FOV to encompass the cerebellar cortex or more lateral regions of the cortex. Finally, mini-mScopes could be designed to incorporate miniaturized amplifiers for integrating chronically implanted recording electrodes for simultaneous mesoscale imaging and deep brain neural recordings, or to interface with electrodes incorporated in the See-Shells for electrocorticography (ECoG)[42].

METHODS

Mini-mScope design fabrication and assembly

Design: The mini-mScope was designed using a computer-aided design (CAD) program (SolidWorks 2018, Dassault Systèmes). The top and bottom housing were CNC milled from Delrin. The illumination module housings were 3D printed using a desktop

Author Manuscript Author Manuscript Author Manuscript Author Manuscript

stereolithography (SLA) printer (Form 2, Formlabs Inc.) with black polymethylmethacrylate (PMMA) resin (RS-F2-GPBK-04, Formlabs Inc.). 1.5 mm x 2 mm x 1 mm copper plates were soldered to the large pad on the backs of the LEDs to act as heatsinks (Supplementary Fig. 1a). A blue LED (LUXEON Rebel Color Blue 470 nm, Digikey Inc.) and custom diced bandpass excitation filter (450-490 nm, 3 mm x 3 mm x 1 mm, ET 470/40x, Chroma) were installed into an illumination module using UV-curable optical glue (AA352 Light Cure Adhesive, LOCTITE) (Supplementary Fig. 1b–c). Three such modules were assembled and mounted in the bottom housing of the mini-mScope, and the three blue LEDs were serially wired using 29-gauge wires (Low-Voltage High-Temperature Black, Red Wire with FEP Insulation 29 Wire Gauge, McMaster-Carr) (Supplementary Fig. 1d). UV-curable black resin was applied to the back of each blue LED to encapsulate the wires for stabilization. A biconvex lens (3 mm diameter, 4.5 mm focal length, 0.33 NA, Achromatic Doublet Lens, 47-721, Edmund Optics) with a numerical aperture of 0.33 and effective focal length of 4.50 was gently inserted and press fit into the circular slot at the top of the bottom housing, followed by mounting a custom diced bandpass emission filter (500-550 nm, 4 mm x 4 mm x 1 mm, ET 525/50m, Chroma) (Supplementary Fig. 1e–f). A green LED (LUXEON Rebel Color Green 530nm, Digikey Inc.) was bonded to the green LED slot of the bottom housing using cyanoacrylate glue (Professional Super Glue, LOCTITE) (Supplementary Fig. 1g). A CMOS sensor (Miniscope CMOS PCB, Labmaker) was fastened to the top housing using M1 Thread-Forming Screws (96817A704, McMaster Carr). The top housing was slid onto the rectangular shaft of the bottom housing, and the focusing was adjusted and then fixed using 316 Stainless Steel 0-80 screws (91735A262, McMaster Carr) (Supplementary Fig. 1h). Two circular neodymium magnets (B07C8ZZ2K9, Amazon) were bonded to the bottom surface of the bottom housing with cyanoacrylate glue (Supplementary Fig. 1i).

Wiring: A single coax cable (50 Ω co-axial silicone rubber jacketed cable, Cooner Wire) was used to connect the CMOS sensor to the main DAQ board (Miniscope DAQ PCB, Labmaker). For synchronized illumination of alternate frames with blue and green light, the external trigger output from the CMOS sensor DAQ was sent to a microcontroller (Teensy 3.5, PJRC). At each odd frame, a microcontroller sent a 3.3V transistor-transistor logic (TTL) pulse to a power metal oxide field effect transistor (MOSFET IRL520, Digikey) relay to turn on the three blue LEDs for 20 ms. At each even frame, a second TTL pulse lasting 4 ms was sent to a dedicated MosFET powering the green LED. The wires powering the LEDs were routed through a circular hole in the top housing and then a commutator (Carousel Commutator 1x DHST 2x LED, Plexon) for strain relief. High wattage resistors were used in the switching circuit (Supplementary Fig. 2) and the power supplies for each illumination source were used to modulate the current delivered to the LEDs and tune light illumination output during *in vivo* experiments.

Animals

All animal experiments were conducted in accordance with protocols approved by the University of Minnesota's Institutional Animal Care and Use Committee (IACUC) and the University of Lethbridge's Animal Care Committee. C57BL/6J, Thy1-GCaMP6f, and Emx-CaMKII-Ai85 mice were used in the experiments. Both male and female mice were used,

Author Manuscript Author Manuscript Author Manuscript Author Manuscript

aged 8-30 weeks. Mice were housed in a 14-hour light / 10 hour dark cycle at 20-23 C and 30-70% relative humidity with ad libitum access to food and water.

See-Shell Preparation and Implantation

See-Shell and protective cap preparation: The See-Shell implant was assembled using the technique adapted from our previous work[24]. Briefly, the frame of the See-Shell and protective cap were 3D printed using a desktop SLA printer with UV-curable black PMMA resin. A 50 μm thick PET film (Melinex 462, Dupont Inc.) was bonded to the PMMA frame using quick setting epoxy (ScotchWeld dp100 Plus Clear, 3M Inc.). Two circular neodymium magnets were inserted into the slots on the implant and bottom surface of the protective cap and fixed using cyanoacrylate glue. An 0-80 nut was inserted into the hole in the posterior tab of the implant (Brass Hex Nut, 0-80 Thread Size, McMaster-Carr).

Surgical Implantation

See-Shell implantation: Mice were administered 2 mg/kg of slow release Buprenorphine (Buprenorphine SR-LAB, Zoopharm Inc.) and 2 mg/kg of Meloxicam for analgesia and inflammation prevention, respectively. Mice were anesthetized in an induction chamber containing 1-5% isoflurane in pure oxygen. The scalp was shaved and sterilized, followed by application of sterile eye ointment (Puralube, Dechra Veterinary Products) to the eyes. Mice were then transferred and affixed to either a standard rodent stereotax (Model 900LS, Kopf Inc.) or an automated robotic surgery platform, the Craniobot[43,44]. The scalp above the dorsal cortex was excised using surgical scissors and fascia was removed using a 0.5 mm micro-curette (10080-05, Fine Science Tools). A large craniotomy over the dorsal cortex was performed either manually using a high-speed dental drill or automatically using the Craniobot. Once the skull was removed, the exposed brain was immediately covered in a gauze pad soaked in sterile saline to keep the brain hydrated.

The See-Shell implant was sterilized by soaking in 70% ethanol for 2 minutes, followed by thorough rinsing with sterile saline. The gauze pad on the brain was removed and excess blood from the craniotomy was cleared using cotton tip applicators (823-WC, Puritan). The See-Shell implant was gently placed on the skull, and the area of the skull surrounding the See-Shell was dried using cotton tipped applicators. Surgical glue (Vetbond, 3M Inc.) was applied around the edge of the See-Shell followed by opaque dental cement (Metabond, Parkell Inc.) to adhere it to the skull. The cement fully cured before the protective cap was magnetically attached. Mice recovered on a heated recovery pad (72-0492, Harvard Apparatus Inc.) until fully ambulatory before returning to a clean home cage. Post-operative analgesia and anti-inflammatory drugs were administered for up to 72 hours post-surgery. Mice were subsequently allowed to recover for 7 days prior to imaging experiments.

Intact skull surgical preparation for mouse shown in Figure 1d followed the protocol described previously[45]. Intact skull imaging using the mini-mScope followed along similar lines with minor modifications, as described in Supplementary Note 4.

Electrophysiology: In experiments where we performed simultaneous electrophysiology and mesoscale imaging, a hippocampal electrode was implanted through a hole outside the

Author Manuscript Author Manuscript Author Manuscript Author Manuscript

area of the See-Shell craniotomy. Briefly, a bipolar (tip separation of 500 μm) electrode made from Teflon-coated stainless-steel wire (bare diameter 50.8 μm) was placed in the pyramidal layer of the right dorsal hippocampus. It was inserted posterior to the occipital suture at a 33-degree angle (with respect to the vertical axis) according to the following coordinates relative to bregma: ML: 2.3 mm; dorsoventral (DV): 2.2 to 2.5 mm. The position of the electrode tips was confirmed using an audio monitor (AM8C #72x32B, Grass Instrument Co.). After electrode implantation, the craniotomy was performed and the See-Shell was implanted on the skull as described above.

Benchtop characterization optical imaging performance of the mini-mScope

Resolution testing: A transparent 1951 USAF test target was cut to isolate each group and the center of the target was placed onto a 3D printed inverse mold of the See-Shell contour with markings for 8 different test locations in the FOV. A See-Shell implant was pressed onto the inverse mold with the target and images were taken in each location (Fig. 1e).

Illumination profile: To measure the uniformity of illumination, a custom 3D printed acrylic container was filled with fluorescein dye (10% v/v, F2456, Sigma Aldrich Inc.) infused 3% agar gel. The See-Shell implant was placed on the container such that the entire bottom surface of the See-Shell was uniformly coated with fluorescent gel. The mini-mScope was attached to the See-Shell and single images were acquired. The current delivered to the LEDs was modulated using power supplies in the switching circuit (Supplementary Fig. 2) to eliminate FOV saturation. The captured images were analyzed in MATLAB 2019a (MathWorks, Inc.) using custom code.

LED switching dynamics and LED power stability testing: To test LED stability, the blue LEDs were pulsed at 100 Hz and output light was measured using a photoresistor (NSL-19M51, Advanced Photonix). The output voltage of the photoresistor was analyzed in MATLAB to calculate the mean intensity across the FOV (Supplementary Note 2).

Focusing and calibration of mini-mScope

Before every experiment, mice were lightly anesthetized (0.5-1% isoflurane in pure oxygen) and head-fixed in a stereotax to clean the See-Shell surface of any debris. The mini-mScope was then securely mounted on the implant. The green LED was switched on and the position of the top housing relative to the bottom housing was manually adjusted until the area around the midline was in focus. The adjustment screw was tightened to secure it in place. Once focused, the three blue LEDs and green LED were alternately pulsed, and their intensities were adjusted by modulating the power delivered to the LEDs using each power supply (Supplementary Fig. 2).

In vivo calcium imaging in anesthetized mice

In vivo calcium imaging experiments were performed to compare mini-mScope imaging capabilities to a conventional macroscope. Mice were lightly anesthetized and affixed to a custom stereotaxic setup under a macroscope (Leica MZ10F, Leica AG). Images from the macroscope were captured using a sCMOS camera (Orca Flash 4.0, Hamamatsu Inc.).

Author Manuscript Author Manuscript Author Manuscript Author Manuscript

Bright field images were first captured to assess the quality of the cranial window followed by epifluorescence imaging. Blue illumination was captured at 8 bits and 15 Hz in the mini-mScope. The sCMOS camera was configured to acquire images at 8 bits and 30 fps. In the final imaging analysis, every other frame was discarded to ensure an effective acquisition rate of 15 Hz. The mini-mScope was attached immediately after image acquisition from the macroscope and 4 minutes of spontaneous calcium activity were captured. To evaluate a neural response to sensory stimuli, a 1 s vibrational stimulus was provided to the hindlimb using a 3V DC mini vibration motor (A00000464, BestTong) at 100 Hz. For visual stimulus, a white LED was positioned ~ 2 cm from the left eye of the mouse to cover the fovea in the visual field. 100 ms flashes of light were presented after ensuring stimulus delivery was confined to the left eye.

Open field and social behavior experiments

Mice underwent acclimatization for 3-5 days in which an experimenter handled each mouse for 5-15 minutes. The mice were fitted with a mini-mScope replica with the same weight as a fully assembled mini-mScope during the handling period. For experimentation, the mini-mScope was fitted onto the mouse, which was quickly transferred to an open field arena. Experimental trials lasted 6 minutes, including a two-minute period to allow the LEDs to warm up to their maximum intensity. During social behavior experiments, a C57BL/6 mouse of the same sex was gently introduced into the arena by an experimenter 4 minutes after initiation of the trial.

Sleep recording experiment

Mice were habituated for 7 days in the recording setup with the mini-mScope mounted on their head. Each mouse was recorded for two sessions, each lasting two hours. Hippocampal LFP was amplified (×1000) and filtered (0.1-300 Hz) using a Grass P5 Series AC amplifier (Grass Instrument Co.) and was sampled at 1 kHz using a data acquisition system (Axon Instruments). A camera (Camera Module V2 #E305654, Raspberry Pi) was used to record behavior during the recording.

Data Analysis

Behavior video analysis: Videos of mouse behavior were captured in .avi format using an overhead camera (ELP_USB8MP02G-L75, ELP). Mice were tracked using either Zebtrack[46] software in MATLAB or using Deeplabcut[47]. Each trial was manually verified to ensure tracking accuracy. A 17 cm square area was defined at the center of the arena as the ‘open field’. To segment the behavior based on different behavior epochs, four researchers manually scored behavior with 1 s precision based upon whether the mouse with the mini-mScope was moving, still, grooming or rearing, and whether the mice engaged in social behavior indicated by touching in “contact” and “no contact” epochs. Scoring data was processed if there was consensus with at least 3 researchers.

Imaging data pre-processing: Data from the CMOS sensor was captured in .avi format (RGB, 480x752 image size) and contained alternate blue and green channel data. A custom MATLAB script was used to convert the videos from RGB to grayscale and truncated to exclude the 2-minute LED warmup period at the start of each trial. The resulting video was

Author Manuscript Author Manuscript Author Manuscript Author Manuscript

segmented into individual blue and green channel videos. Blue and green frames were binned using a bilinear spatial binning algorithm in MATLAB. Pixels in each channel were corrected for global illumination fluctuations using a correction algorithm[3] and were spatially filtered using a custom weighted spatial filtering algorithm.

ΔF/F calculations: Intensity values from the selected ROIs from the blue and green illumination videos were computed using FIJI 2.1.0/ImageJ 1.53c.[48] Change in fluorescence for both GCaMP and reflectance signals were calculated over a baseline average across the whole time series.

Hemodynamic correction: The green channel ΔF/F traces were filtered using a zero-phase Chebyshev lowpass filter (cutoff frequency of 0.15 Hz). The blue ΔF/F and filtered green ΔF/F traces were used to perform hemodynamic correction as described previously[7]. The hemodynamic corrected traces were filtered using a zero-order phase Chebyshev bandpass filter (cutoff frequencies of 0.1 Hz and 5 Hz).

Open field experiments: The videos acquired from freely moving animals were corrected for lateral motion artifacts using MoCo rigid motion correction[26]. The first frame of the video was used as the template for motion correction. Parameters used for the MoCo plugin were w = 40 and a down sample value = 0.5. Log files of pixel displacements and a corrected output video were generated.

The time stamp data from the Miniscope v3 software contains a list of frames captured by the behavior camera and CMOS sensor. To mitigate frame pacing issues with the CMOS sensor, only frames within ±10% of the specified frame rate were kept. To address the frame dropping issues with the behavior camera (usually dropped ~400/10800 frames), common frames that exist in the CMOS video and behavior camera video were stored. The resulting data was compared to the manually scored behavior data to find the intersection between these frame data sets. Finally, this list was searched to find points with consecutively paired blue and green frames to be used for hemodynamic corrections.

Seed-pixel correlation maps: Cortical regions of interest were selected within each video trial by removing the background and areas with high vasculature (Fig. 4e) and seed pixels within 6 regions (motor cortex (M1), frontal lobe (FL), barrel cortex (BC), retrosplenial cortex (RSC), visual cortex (VC), hind limb (HL)) were selected for further analysis. Cortical regions were selected by imposing a post-surgery image onto a map extracted from Brain Explorer 2 [49] and registering regions based upon static landmarks on the implant with respect to Bregma and Lamda. Seed pixel correlation maps were generated using Pearson's correlation coefficient (PCC) to compare the correlation between a desired seed pixel and other pixels in the FOV. Data from the manual scoring (Fig. 4c and d) was used to generate a list of frame numbers where the mouse was either moving or still. To calculate PCC during these discontinuous epochs of time, a moving window of 1 s with a 0.5 s sliding window was incorporated between small clusters of continuous behavior. The PCC between the seed pixel trace and every other pixel in the desired regions of the cortex was calculated for each window length portion. The mean of all the PCCs was computed and stored as the PCC value for each pixel in the FOV. This process was repeated for each trial

Author Manuscript Author Manuscript Author Manuscript Author Manuscript

and mouse to generate representative seed pixel maps for one trial as shown in Figure 4f. The PCC value between the chosen seed pixels were averaged across all trials in spontaneous free behavior to generate the inter-seed correlational plots shown in Figure 4h. To measure the change in activity across the left hemisphere where the seed pixels were chosen, the percentage of pixels in this ROI with PCC $r > 0.5$ was averaged across trials (Fig. 4g). Similar analysis was performed for social interaction experiments.

Glutamate data preprocessing: Raw data of spontaneous glutamate activity was preprocessed based on the following steps: First, the time series of each pixel was filtered using a zero-phase bandpass Chebyshev filter between 0.1 and 5 Hz. Then a baseline signal was calculated by averaging all the frames, and the fluorescence changes were quantified as $\Delta F/F \times 100$, where F is the filtered signal. To reduce spatial noise, images were filtered by a Gaussian kernel (5×5 pixels, sigma = 1).

State scoring: Behavioral states were scored visually using hippocampal LFP and movement signal in 10 s epochs. Movement signals were calculated using a previously described algorithm[50]. Active wakefulness (aW) was characterized by theta hippocampal activity and high movements. Quiet wakefulness (qW) was characterized by theta hippocampal activity and minimum movement. NREM sleep (N) was characterized by large irregular activity in hippocampus and no movement. REM sleep (R) was characterized by theta hippocampal activity and no movement.

Correlation analysis: A uniform meshgrid with ~1.2 mm distance between its points was laid on the field of view and signal at each ROI (0.2 mm^2) was calculated. Quiet wake, NREM sleep and REM sleep were scored for each recording based on above criteria and Pearson correlation coefficients were calculated between each ROIs during qW, NREM and REM. For comparison in Figure 4f, correlation matrices were averaged across all ROIs.

Statistics and Reproducibility

Raw cortical images, similar to the representative images in Figure 1c and d, have been taken in all mice and can be reproduced throughout figures in the manuscript. Sample sizes for all numerical data in graphs have a minimum n = 3 and statistical tests were performed with a minimum n = 5.

Supplementary Material

Refer to Web version on PubMed Central for supplementary material.

ACKNOWLEDGEMENTS

SBK acknowledges funds from the Mechanical Engineering department, College of Science and Engineering, MnDRIVE RSAM initiative of the University of Minnesota, Minnesota department of higher education, National Institutes of Health (NIH) 1R21NS103098-01, 1R01NS111028, 1R21NS112886, RF1NS113287 and 1R21NS111196. LG was supported by the University of Minnesota Informatics Institute's (UMII) graduate fellowship. DS was supported by the University of Minnesota's Diversity of Views and Experiences (DOVE) fellowship. MLR was supported by 1R21NS103098-01-01S1.

Author Manuscript Author Manuscript Author Manuscript Author Manuscript

REFERENCES

1. Chen T-W et al. Ultrasensitive fluorescent proteins for imaging neuronal activity. Nature 499, 295–300 (2013). [PubMed: 23868258]
2. Daigle TL et al. A Suite of Transgenic Driver and Reporter Mouse Lines with Enhanced Brain-Cell-Type Targeting and Functionality. Cell 174, 465–480 (2018). [PubMed: 30007418]
3. Vanni MP & Murphy TH Mesoscale transcranial spontaneous activity mapping in GCaMP3 transgenic mice reveals extensive reciprocal connections between areas of somatomotor cortex. J. Neurosci 34, 15931–15946 (2014). [PubMed: 25429135]
4. Allen WE et al. Global Representations of Goal-Directed Behavior in Distinct Cell Types of Mouse Neocortex. Neuron 94, 891–907 (2017). [PubMed: 28521139]
5. Wekselblatt JB, Flister ED, Piscopo DM & Niell CM Large-scale imaging of cortical dynamics during sensory perception and behavior. J. Neurophysiol 115, 2852–66 (2016). [PubMed: 26912600]
6. Makino H et al. Transformation of Cortex-wide Emergent Properties during Motor Learning. Neuron 94, 880–890 (2017). [PubMed: 28521138]
7. Musall S, Kaufman MT, Juavinett AL, Gluf S & Churchland AK Single-trial neural dynamics are dominated by richly varied movements. Nat. Neurosci 22, 1677–1686 (2019). [PubMed: 31551604]
8. Gilad A & Helmchen F Spatiotemporal refinement of signal flow through association cortex during learning. Nat. Commun 11, 1744 (2020). [PubMed: 32269226]
9. Mohajerani MH et al. Spontaneous cortical activity alternates between motifs defined by regional axonal projections. Nat. Neurosci 16, 1426–1435 (2013). [PubMed: 23974708]
10. Ferezou I et al. Spatiotemporal Dynamics of Cortical Sensorimotor Integration in Behaving Mice. Neuron 56, 907–23 (2007). [PubMed: 18054865]
11. Niu Y et al. Generation of gene-modified cynomolgus monkey via Cas9/RNA-mediated gene targeting in one-cell embryos. Cell 156, 836–843 (2014). [PubMed: 24486104]
12. Pinto L et al. Task-Dependent Changes in the Large-Scale Dynamics and Necessity of Cortical Regions. Neuron 104, 810–824 (2019). [PubMed: 31564591]
13. Murphy TH et al. High-throughput automated home-cage mesoscopic functional imaging of mouse cortex. Nat. Commun 7, 11611 (2016). [PubMed: 27291514]
14. Meyer AF, O'Keefe J & Poort J Two Distinct Types of Eye-Head Coupling in Freely Moving Mice. Curr. Biol 30, 2116–2130.e6 (2020). [PubMed: 32413309]
15. Juczewski K, Koussa JA, Kesner AJ, Lee JO & Lovinger DM Stress and behavioral correlates in the head-fixed method: stress measurements, habituation dynamics, locomotion, and motor-skill learning in mice. Sci. Rep 10, 12245 (2020). [PubMed: 32699235]
16. Aghajan ZM et al. Impaired spatial selectivity and intact phase precession in two-dimensional virtual reality. Nat. Neurosci 18, 121–128 (2015). [PubMed: 25420065]
17. Ghosh KK et al. Miniaturized integration of a fluorescence microscope. Nat. Methods 8, 871–878 (2011) doi:10.1038/nmeth.1694. [PubMed: 21909102]
18. Zong W et al. Fast high-resolution miniature two-photon microscopy for brain imaging in freely behaving mice. Nat. Methods 14, 713 (2017). [PubMed: 28553965]
19. Skocek O et al. High-speed volumetric imaging of neuronal activity in freely moving rodents. Nat. Methods 15, 429–432 (2018). [PubMed: 29736000]
20. Scott BB et al. Imaging Cortical Dynamics in GCaMP Transgenic Rats with a Head-Mounted Widefield Macroscope. Neuron 100, 1045–1058 (2018). [PubMed: 30482694]
21. Namiki S, Sakamoto H, Iinuma S, Iino M & Hirose K Optical glutamate sensor for spatiotemporal analysis of synaptic transmission. Eur. J. Neurosci 25, 2249–59 (2007). [PubMed: 17445223]
22. Marvin JS et al. An optimized fluorescent probe for visualizing glutamate neurotransmission. Nat. Methods 10, 162–170 (2013). [PubMed: 23314171]
23. Dana H et al. Thy1-GCaMP6 transgenic mice for neuronal population imaging in vivo. PLoS One 9, (2014).
24. Ghanbari L et al. Cortex-wide neural interfacing via transparent polymer skulls. Nat. Commun 10, 1500 (2019). [PubMed: 30940809]

Author Manuscript Author Manuscript Author Manuscript Author Manuscript

25. Ma Y et al. Resting-state hemodynamics are spatiotemporally coupled to synchronized and symmetric neural activity in excitatory neurons. Proc. Natl. Acad. Sci. U. S. A 113, E8463–E8471 (2016). [PubMed: 27974609]
26. Dubbs A, Guevara J & Yuste R moco: Fast motion correction for calcium imaging. Front. Neuroinform (2016) doi:10.3389/fninf.2016.00006.
27. Dash MB, Douglas CL, Vyazovskiy VV, Cirelli C & Tononi G Long-term homeostasis of extracellular glutamate in the rat cerebral cortex across sleep and waking states. J. Neurosci 29, 620–629 (2009). [PubMed: 19158289]
28. Abadchi JK et al. Spatiotemporal patterns of neocortical activity around hippocampal sharp-wave ripples. Elife 9, (2020).
29. Patti CL et al. Effects of sleep deprivation on memory in mice: Role of state-dependent learning. Sleep 33, 1669–1679 (2010). [PubMed: 21120129]
30. Colavito V et al. Experimental sleep deprivation as a tool to test memory deficits in rodents. Front. Syst. Neurosci 7, (2013).
31. Mohajerani MH, McVea DA, Fingas M & Murphy TH Mirrored bilateral slow-wave cortical activity within local circuits revealed by fast bihemispheric voltage-sensitive dye imaging in anesthetized and awake mice. J. Neurosci 30, 3745–3751 (2010). [PubMed: 20220008]
32. Li P et al. Measuring Sharp Waves and Oscillatory Population Activity With the Genetically Encoded Calcium Indicator GCaMP6f. Front. Cell. Neurosci 13, 274 (2019). [PubMed: 31275115]
33. Dana H et al. High-performance calcium sensors for imaging activity in neuronal populations and microcompartments. Nat. Methods 16, 649–657 (2019). [PubMed: 31209382]
34. Madisen L et al. Transgenic mice for intersectional targeting of neural sensors and effectors with high specificity and performance. Neuron 85, 942–958 (2015). [PubMed: 25741722]
35. Dawson TM, Golde TE & Lagier-Tourenne C Animal models of neurodegenerative diseases. Nature Neuroscience vol. 21 1370–1379 (2018). [PubMed: 30250265]
36. Cai DJ et al. A shared neural ensemble links distinct contextual memories encoded close in time. Nature 534, 115–118 (2016). [PubMed: 27251287]
37. Juneau J, Duret G, Robinson J & Kemere C Enhanced Image Sensor Module for Head-Mounted Microscopes*. in Proceedings of the Annual International Conference of the IEEE Engineering in Medicine and Biology Society, EMBS (2018). doi:10.1109/EMBC.2018.8512387.
38. Barbera G, Liang B, Zhang L, Li Y & Lin DT A wireless miniScope for deep brain imaging in freely moving mice. J. Neurosci. Methods 323, 56–60 (2019). [PubMed: 31116963]
39. Valley MT et al. Separation of hemodynamic signals from GCaMP fluorescence measured with wide-field imaging. J. Neurophysiol 123, 356–366 (2020). [PubMed: 31747332]
40. Lerner TN et al. Intact-Brain Analyses Reveal Distinct Information Carried by SNc Dopamine Subcircuits. Cell 162, 635–647 (2015). [PubMed: 26232229]
41. Dana H et al. Sensitive red protein calcium indicators for imaging neural activity. Elife 5, (2016).
42. Donaldson PD, Ghanbari L, Rynes ML, Kodandaramaiah SB & Swisher SL Inkjet-Printed Silver Electrode Array for in-vivo Electrocorticography. in International IEEE/EMBS Conference on Neural Engineering, NER vols 2019-March (2019).
43. Ghanbari L et al. Craniobot: A computer numerical controlled robot for cranial microsurgeries. Sci. Rep 9, 1023 (2019). [PubMed: 30705287]
44. Rynes ML et al. Assembly and operation of an open-source, computer numerical controlled (CNC) robot for performing cranial microsurgical procedures. Nat. Protoc 15, 1992–2023 (2020). [PubMed: 32405052]
45. Silasi G, Xiao D, Vanni MP, Chen ACN & Murphy TH Intact skull chronic windows for mesoscopic wide-field imaging in awake mice. J. Neurosci. Methods 267, 141–149 (2016). [PubMed: 27102043]
46. Pinheiro-da-Silva J, Fernandes Silva P, Nogueira M & Luchiari A ESM 1. (2016).
47. Mathis A et al. DeepLabCut: markerless pose estimation of user-defined body parts with deep learning. Nat. Neurosci 21, 1281–1289 (2018). [PubMed: 30127430]
48. Schindelin J et al. Fiji: An open-source platform for biological-image analysis. Nature Methods vol. 9 676–682 (2012). [PubMed: 22743772]

Author Manuscript Author Manuscript Author Manuscript Author Manuscript

49. Lau C et al. Exploration and visualization of gene expression with neuroanatomy in the adult mouse brain. BMC Bioinformatics 9, 153 (2008). [PubMed: 18366675]

50. Singh S, Bermudez-Contreras E, Nazari M, Sutherland RJ & Mohajerani MH Low-cost solution for rodent home-cage behaviour monitoring. PLoS One 14, e0220751 (2019). [PubMed: 31374097]

Author Manuscript Author Manuscript Author Manuscript Author Manuscript

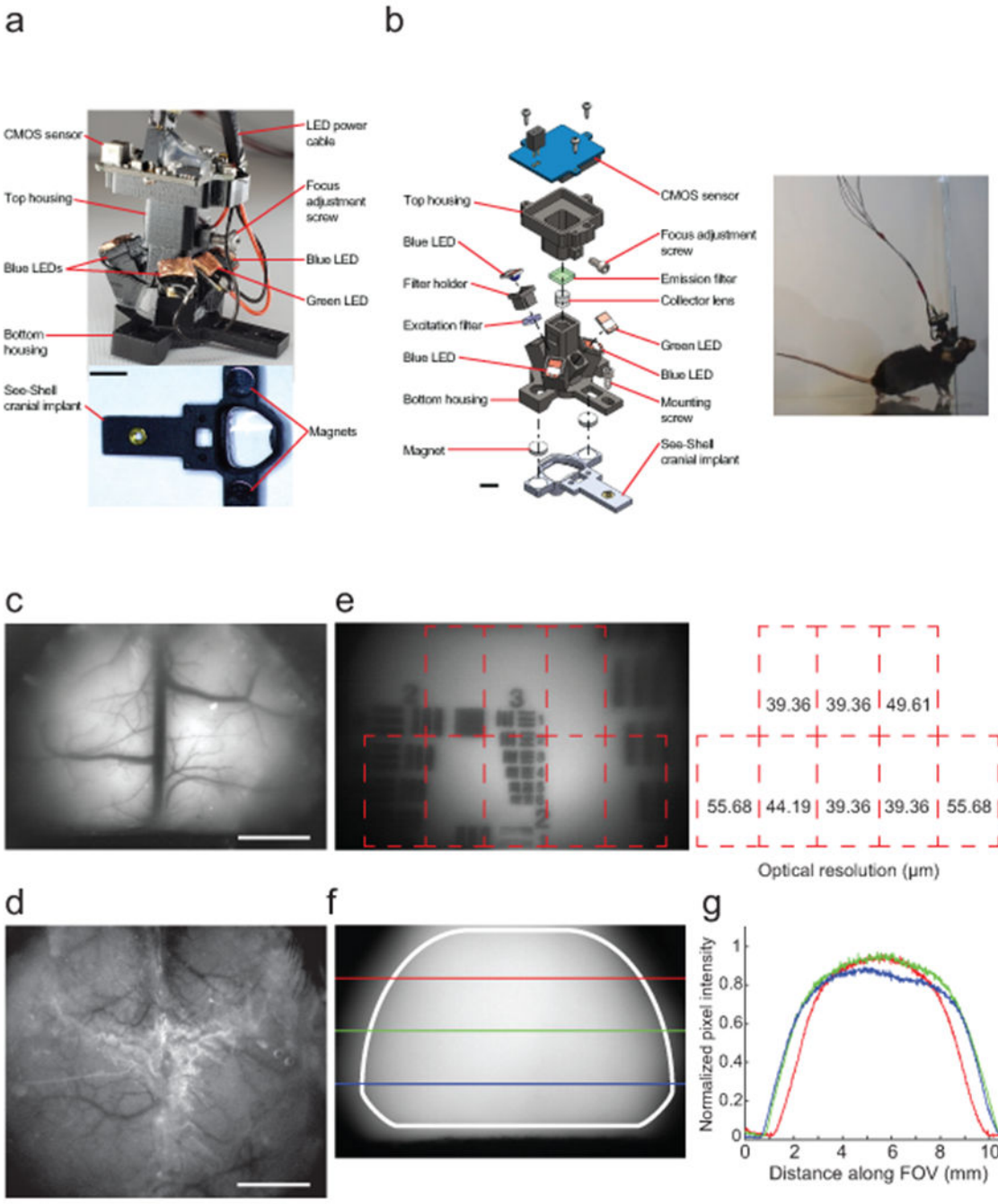

Figure 1: mini-mScope: A miniaturized head-mounted device for whole-cortex mesoscale activity mapping in freely behaving mice:

(a) Photograph of the fully assembled mini-mScope and the corresponding See-Shell implant. Scale bar, 5 mm **(b)** *Left:* Computer-aided design (CAD) rendering of the mini-mScope showing the internal components. The device is attached to the See-Shell implant via magnets. Three blue LEDs are attached to a filter holder that has a 480 nm excitation filter to excite GCaMP6f in the cortex. The green LED is used to obtain reflectance measurements for hemodynamic correction. Resulting emission signals (~520 nm) are

Author Manuscript Author Manuscript Author Manuscript Author Manuscript

focused through a collector lens and passed through an emission filter onto a CMOS sensor that can be manually focused. Scale bar indicates 5 mm. *Right:* A still image of a mouse bearing the mini-mScope and engaging in natural behaviors. **(c)** Fluorescence image of the whole dorsal cortex of a Thy1-GCaMP6f mouse captured by the mini-mScope. Scale bar indicates 2 mm. Image representative of n = 29 mice. **(d)** Comparative image of a head-fixed Thy1-GCcaMP6f mouse imaged using a standard epifluorescence macroscope through an intact-skull preparation. Scale bar indicates 2 mm. Image representative of n = 2 mice. **(e)** *Left:* Resolution test target overlaid onto the mini-mScope FOV. *Right:* Resolutions obtained within each specified grid. **(f)** Image of fluorescein dye infused agar phantom captured by the mini-mScope. Colored lines indicate mediolateral sections along which illumination profiles were obtained FOV. **(g)** Plot of normalized illumination profiles from sections denoted in **f**.

Author Manuscript Author Manuscript Author Manuscript Author Manuscript

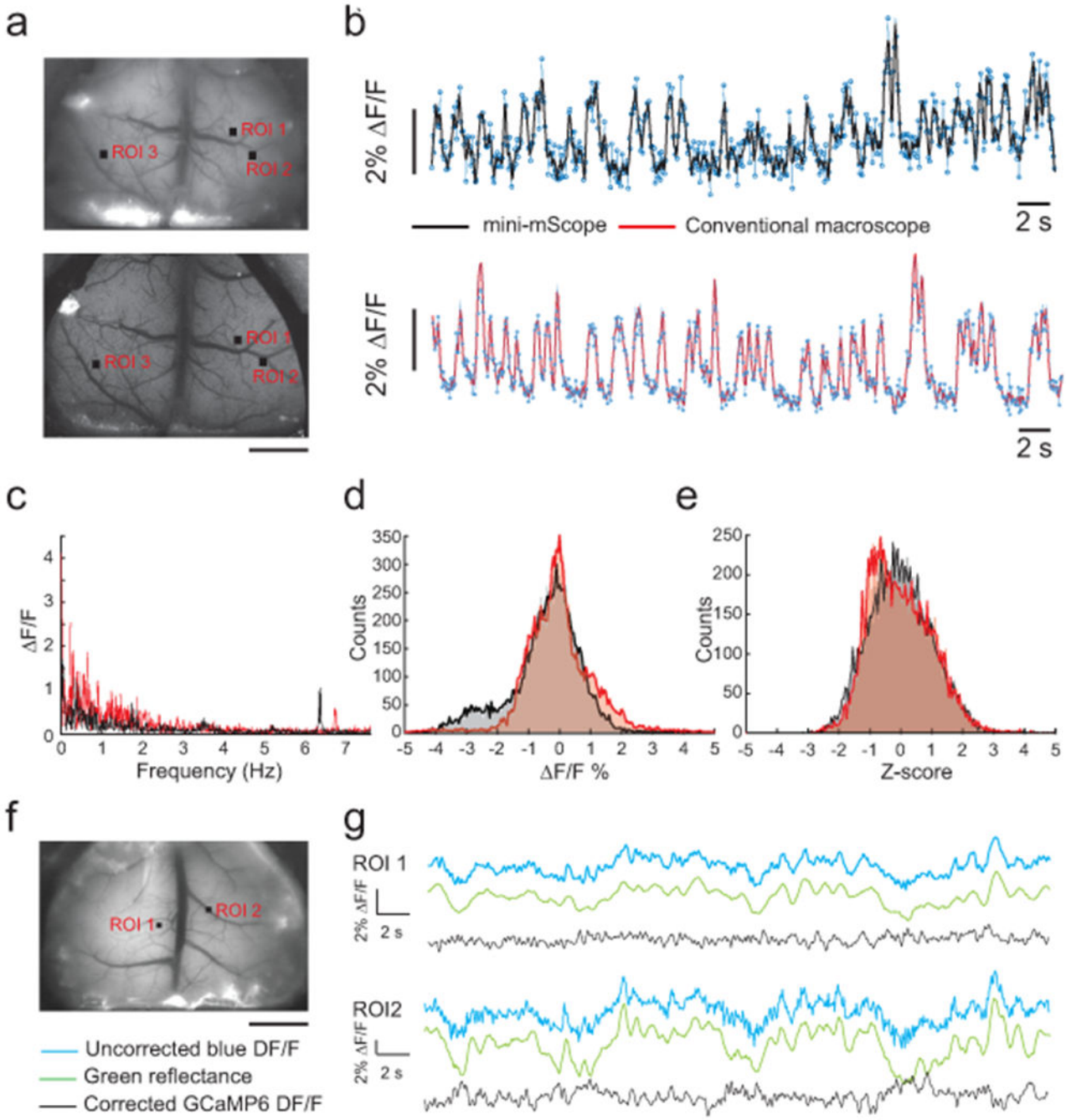

Figure 2: Comparison of calcium dynamics imaged with the mini-mScope to conventional widefield epifluorescence macroscope:

(a) *Top:* Image of the dorsal cortex taken with mini-mScope of a Thy1-GCaMP6f mouse. Image representative of n = 29 mice. *Bottom:* image taken with a conventional widefield epifluorescence macroscope during the same experimental session. Image representative of n = 8 mice. Black squares indicate ROIs selected for ΔF/F traces analyzed in **b-e**. Scale bar indicates 2 mm. **(b)** ΔF/F traces of ROI 1 shown in **a** recorded for 120 seconds. In **(b-e)**, black and red traces indicate filtered traces (Savitzky-Golay filter, 3rd order polynomial, 5

Author Manuscript Author Manuscript Author Manuscript Author Manuscript

point moving average) of ΔF/F recorded from the mini-mScope and the macroscope respectively. Blue traces with markers indicate raw ΔF/F values under 1% isoflurane anesthesia. **(c)** Plot of the ΔF/F versus Frequency obtained by computing the discrete Fourier series of 120s of spontaneous calcium activity recorded under isoflurane anesthesia (from traces shown in **b**.) **(d)** Histogram of ΔF/F values over 2-minute videos captured at the same 1% isoflurane anesthesia conditions with the mini-mScope and the conventional macroscope in the three ROIs indicated in **a**. **(e)** Histogram of z-scores of fluorescent intensity values over 2-minute videos captured at the same 1% isoflurane anesthesia conditions with the mini-mScope and the conventional macroscope in the three ROIs indicated in **a**. **(f)** Image of the dorsal cortex taken with mini-mScope of a Thy1-GCaMP6f mouse. Black squares indicate ROIs selected for hemodynamic corrections illustrated in **g**. Scale bar indicates 2 mm. **(g)** Uncorrected ΔF/F, reflectance ΔF/F and the hemodynamic corrected ΔF/F traces for the two ROIs shown in **i**.

Author Manuscript Author Manuscript Author Manuscript Author Manuscript

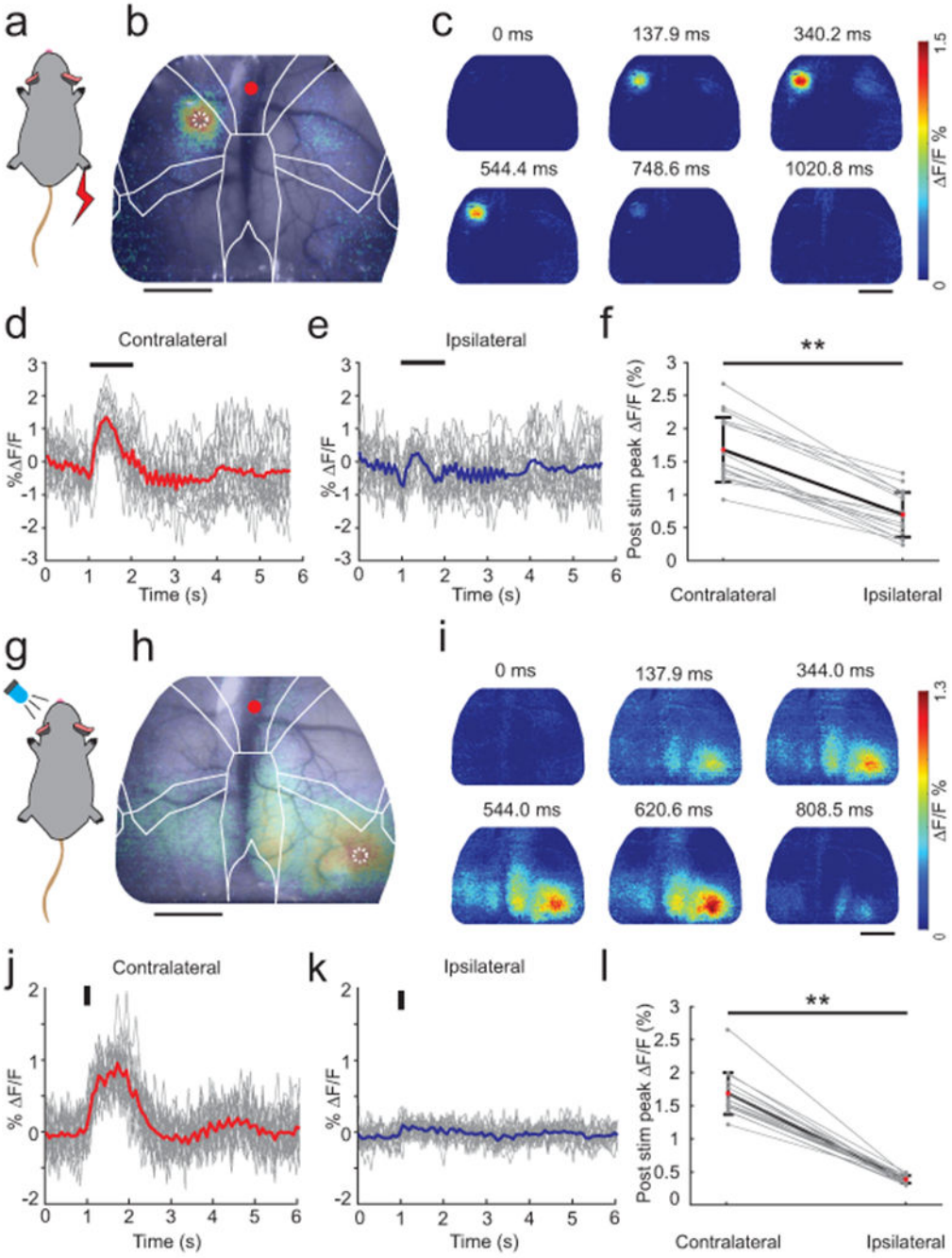

Figure 3: Sensory stimulus evoked responses imaged by the mini-mScope:

(a) Schematic of an anesthetized Thy1-GCaMP6f mouse with a vibrational stimulus applied to the right hind limb. **(b)** Composite of raw grayscale image of the brain and the pseudo-color frame where the largest average ΔF/F occurred within the 1-second stimulus period. White circle indicates ROI analyzed in **d** and **e**. Red dot indicates Bregma. Scale bar 3 mm. **(c)** Montage of average cortical calcium response to the vibration stimulus. Scale bar 2 mm. **(d)** ΔF/F traces of the contralateral ROI drawn in **b**. Red line denotes the average traces, grey lines denotes individual trials. Black bar shows the time and duration of the vibrational

Author Manuscript Author Manuscript Author Manuscript Author Manuscript

stimulus. **(e)** ΔF/F traces of ipsilateral ROI drawn in **b**. Blue line denotes the average response, grey lines denote each individual trial. **(f)** Peak ΔF/F within 1-second of vibration stimulus presentation (n=20 trials in one mouse, data is representative of 3 mice). ** indicates $p < 0.01$, $p = 9.1x10^{-3}$, two-sample t-test. **(g)** Schematic of a mouse with a visual stimulus applied to the left eye. **(h)** Composite of raw grayscale image of the brain and the pseudo-color frame where the largest average ΔF/F occurred within the 1-second stimulus period. White circle indicates ROI analyzed in **j** and **k**. Scale bar 3 mm. Data were acquired in the same mouse as the data in a to f. **(i)** Montage of average cortical calcium response to the visual stimulus. Scale bar 2 mm. **(j)** ΔF/F traces of the contralateral ROI drawn in **h**. Red line denotes the average trace, grey lines denote each individual trial. Black bar shows the time and duration of the visual stimulus. **(k)** ΔF/F traces of ipsilateral ROI drawn in **h**. Blue line denotes average ipsilateral response, grey lines denote individual trials (n=20 trials in one mouse, data is representative of 3 mice). **(l)** Peak ΔF/F within 1-second of visual stimulus presentation. The bolded line corresponds to the average peak response whereas the grey lines indicate the peak response for each trial. ** indicates $p < 0.01$, $p = 1.31x10^{-5}$, two-sample t-test.

Author Manuscript Author Manuscript Author Manuscript Author Manuscript

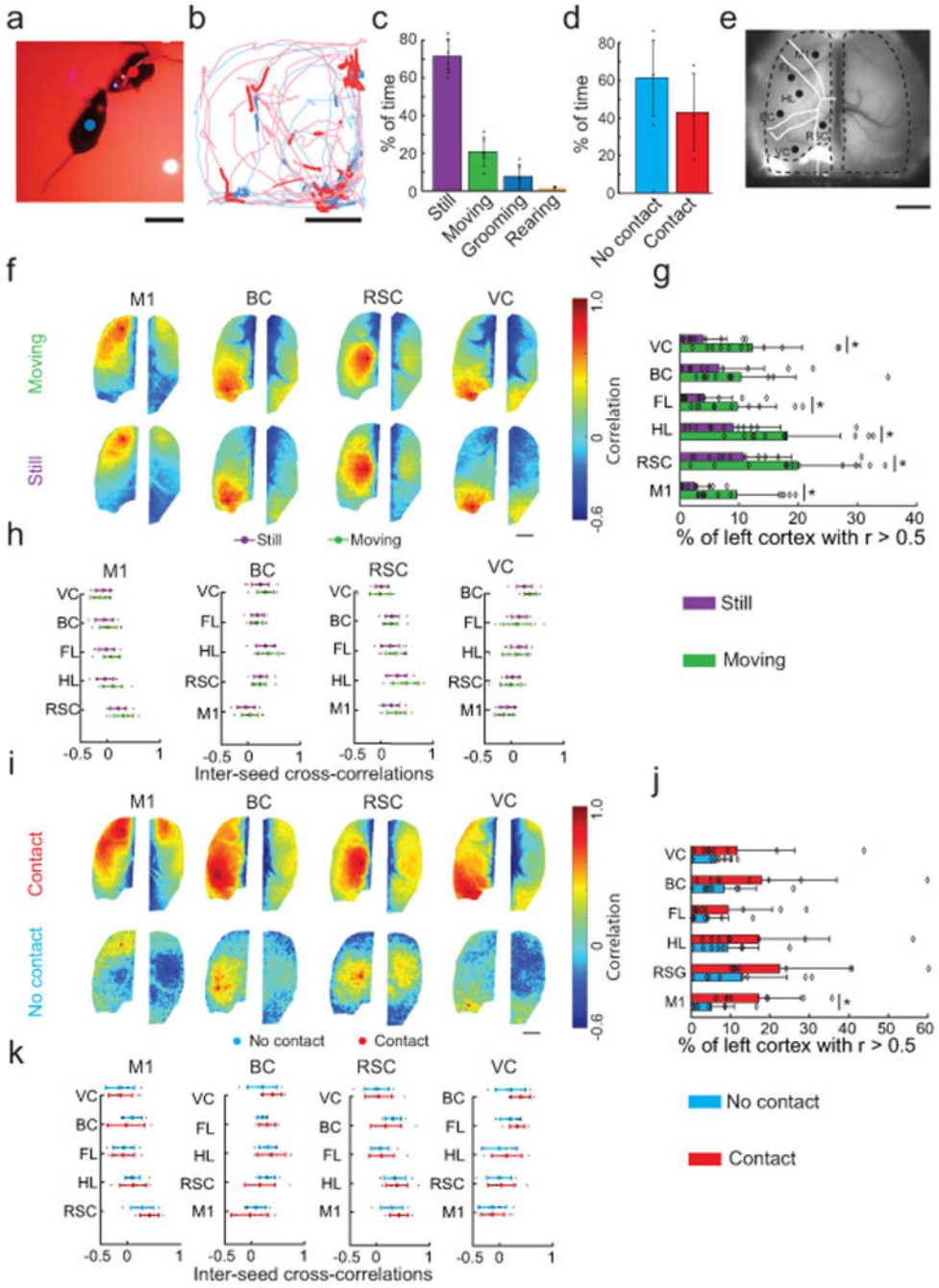

Figure 4: Mesoscale imaging of cortex during free and social behavior:

(a) Photograph of a mouse with a mini-mScope (red dot annotation) interacting with a companion mouse (blue dot annotation). Scale bar, 5 cm. **(b)** Traces of instantaneous locations of the two mice during trial. The segments of darker blue and red indicate positions of the mice when they were within 5 cm of each other. Scale bar, 10 cm. **(c)** Percentage of time spent still, moving, grooming, and rearing during open field behavior (n = 6 trials). **(d)** Percentage of time spent in contact and not in contact with the companion mouse behavior during trials (n = 3 trials). **(e)** Representative image of the cortex with locations of the seed

Author Manuscript Author Manuscript Author Manuscript Author Manuscript

pixels used for analysis in **f-k** are indicated. Scale bar 2 mm. **(f)** Seed pixel correlation maps of motor cortex (M1), barrel cortex (BC), retrospenial cortex (RSC) and visual cortex (VC) during movement and no movement. *Top row:* Average of correlations during 1 s epochs of movement; *bottom row:* Average of correlations during 1 s epochs of no movement. Scale bar 2 mm. **(g)** Change in percentage of hemisphere with $r > 0.5$ with respect to seed pixels analyzed. * indicates $p < 0.05$ ($p = 4.6x10^{-3}$ M1, $p = 6.3x10^{-4}$ FL, $p = 3.8x10^{-3}$ HL, $p = 4.6x10^{-3}$ RSC, $p = 0.10$ BC, $p = 1.1x10^{-3}$ VC, two-sample Mann-Whitney U-test, n = 11 trials, n = 3 mice). Error bars denote mean ± SD. **(h)** Average inter-seed correlations associated with seeds (n = 11 trials, n = 3 mice). Error bars denote mean ± SD. **(i)** Seed pixel correlation maps of M1, BC, RSC and VC during non-social and social behavior epochs. Scale bar 2 mm. **(j)** Percentage of hemisphere with $r > 0.5$ with respect to seed pixels analyzed. * indicates $p < 0.05$ ($p = 0.048$ M1, $p = 0.17$ FL, $p = 0.058$ HL, $p = 0.091$ RSC, $p = 0.082$ BC, $p = 0.37$ VC, two-sample Mann-Whitney U-test, n = 8 trials, n = 8 mice). Error bars denote mean ± SD. **(k)** Average inter-seed correlations associated with the seeds (n= 6 trials, n = 6 mice). Error bars denote mean ± SD.

Author Manuscript Author Manuscript Author Manuscript Author Manuscript

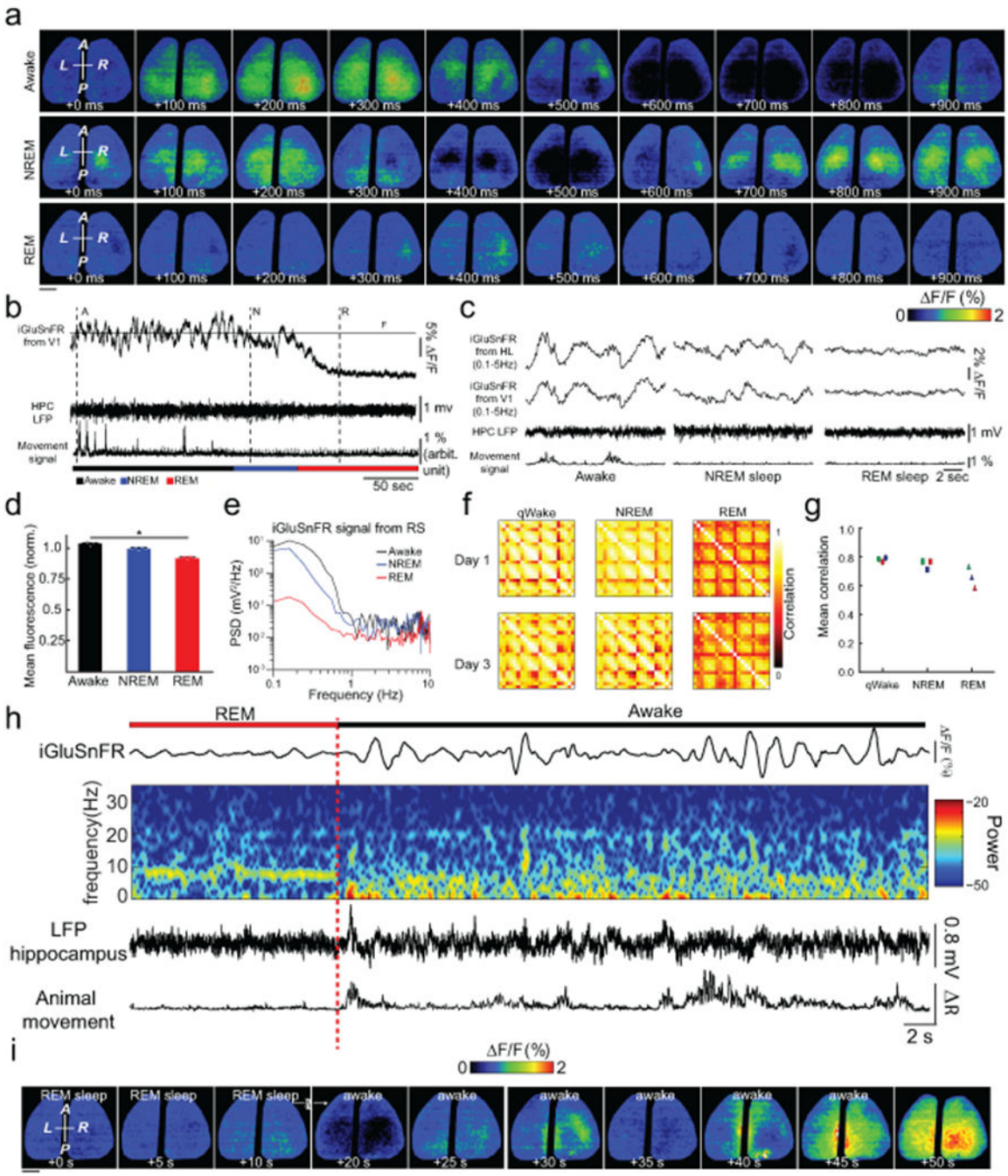

Figure 5: Combined electrophysiological recording and mesoscale imaging of brain activity during wakefulness and sleep:

(a) Montages of change in glutamate activity over 1s period during awake, REM and NREM sleep states. Scale bar 2 mm. **(b)** Representative traces of raw glutamate signals from V1, hippocampal LFP, and video-based movement signals during states of waking, NREM sleep and REM sleep in a freely moving mouse. F_0 is the baseline glutamate signal calculated by averaging the fluorescence over the entire recording time. **(c)** Magnification of glutamate, LFP and movement signals selected in **b**. **(d)** Grouped mean raw glutamate signal from the

Author Manuscript Author Manuscript Author Manuscript Author Manuscript

entire cortex (normalized to baseline) during wakefulness, NREM sleep and REM sleep (n = 3 mice, Friedman paired nonparametric test; post-hoc multiple comparison with Dunn's correction * indicates $p < 0.05$, $p = 0.02$ wakefulness vs REM). **(e)** Spectral analysis of glutamate signal in three states. **(f)** Correlation maps of cortical activity between quiet wakefulness, NREM sleep and REM sleep at two different days. Cortex was divided into 21 ROIs. **(g)** Mean correlation of cortical activity during waking, REM and NREM sleep (n = 3 mice). **(h)** Glutamate activity, hippocampal LFP frequency spectrogram and animal movement tracking during transition from REM to wakefulness **(i)** Montage of cortical glutamate changes during the transition shown in **h**. Scale bar 2 mm.